

Diffusion-Based mmWave Radar Point Cloud Enhancement Driven by Range Images

Ruixin Wu^{1,2,3}, Zihan Li⁴, Jin Wang^{†1,2,3}, Xiangyu Xu^{1,2,3},
Huan Yu^{1,2,3}, Zhi Zheng^{1,2,3}, Kaixiang Huang^{1,2,3} and Guodong Lu^{1,2,3}

Abstract—Millimeter-wave (mmWave) radar has attracted significant attention in robotics and autonomous driving. However, despite the perception stability in harsh environments, the point cloud generated by mmWave radar is relatively sparse while containing significant noise, which limits its further development. Traditional mmWave radar enhancement approaches often struggle to leverage the effectiveness of diffusion models in super-resolution, largely due to the unnatural range-azimuth heatmap (RAH) or bird’s eye view (BEV) representation. To overcome this limitation, we propose a novel method that pioneers the application of fusing range images with image diffusion models, achieving accurate and dense mmWave radar point clouds that are similar to LiDAR. Benefitting from the projection that aligns with human observation, the range image representation of mmWave radar is close to natural images, allowing the knowledge from pre-trained image diffusion models to be effectively transferred, significantly improving the overall performance. Extensive evaluations on both public datasets and self-constructed datasets demonstrate that our approach provides substantial improvements, establishing a new state-of-the-art performance in generating truly three-dimensional LiDAR-like point clouds via mmWave radar.

I. INTRODUCTION

In recent years, mmWave radar has found increasing applications in tasks such as Advanced Driver Assistance Systems (ADAS) and Navigation-Assisted Driving (NOA). Moreover, the application of mmWave radar has also expanded to various robotic systems, including mobile robots [1], unmanned aerial vehicles (UAVs) [2], and unmanned surface vehicles (USVs) [3], [4]. MmWave radar, with its compact structure and robust performance, remains reliable in extreme weather such as rain, snow, and fog, making it an ideal choice for environmental perception in harsh environments.

Despite the obvious advantages of mmWave radar, it is typically used as a supplementary sensor in practical applications, providing supporting information rather than

This work was supported in part by the National Natural Science Foundation of China under Grant 52475033, in part by the “Pioneer” and “Leading Goose” R&D Program of Zhejiang under Grant 2024C01170 and Grant 2023C01070, and in part by the Robotics Institute of Zhejiang University under Grant K12107 and Grant K11805. (Ruixin Wu and Zihan Li contributed equally to this work.)

¹The State Key Laboratory of Fluid Power and Mechatronics Systems, School of Mechanical Engineering, Zhejiang University, Hangzhou 310058, China. ²Zhejiang Key Laboratory of Industrial Big Data and Robot Intelligent Systems, Zhejiang University, Hangzhou 310058, China. ³Robotics Research Center of Yuyao City, Ningbo 315400, China. ⁴State Key Laboratory of Robotics and Systems, Department of Mechatronics Engineering, Harbin Institute of Technology, Harbin 150001, China.

Email: dwjcom@zju.edu.cn

†Corresponding author: Jin Wang.

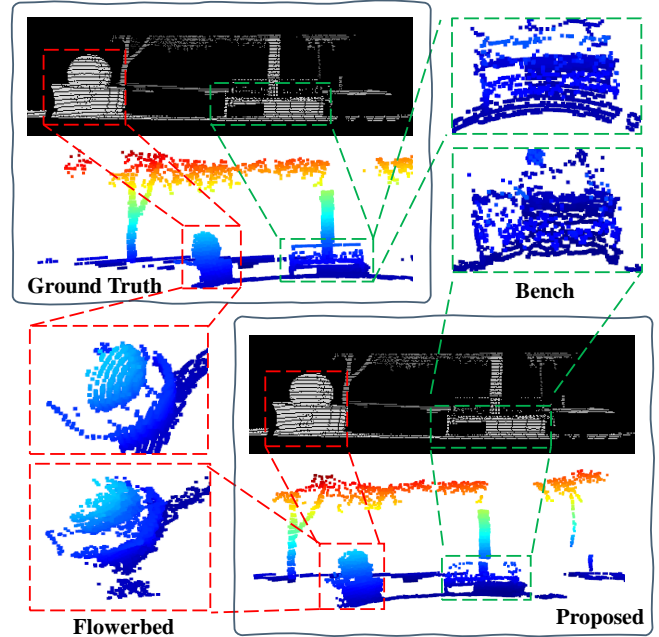


Fig. 1. The comparative demonstration includes LiDAR range images and point clouds, as well as the range images and high-quality millimeter-wave radar point clouds obtained through the proposed method. The red and green dashed boxes highlight the flowerbed and bench in the current scene, respectively. We can easily identify object categories and obtain their geometric structures through range images, demonstrating that range images preserve rich semantic and geometric information. As a proxy representation of point clouds, it enables the knowledge of pre-trained image diffusion models to be fully leveraged in point cloud super-resolution tasks.

being used independently. This situation can be attributed to two primary factors:

- 1) **Cluttered:** In a challenging environment, electromagnetic wave propagation varies significantly due to phenomena such as reflection, scattering, refraction, and diffraction. Furthermore, radiated energy during transmission and reception can create sidelobe signals. These combined effects can lead to the formation of a large number of false point clouds and false targets (ghost points).
- 2) **Sparse:** Compared to LiDAR, radar point clouds are highly sparse, lacking sufficient geometric and detailed information, thus limiting their effectiveness in high-precision tasks like detection, localization, and mapping.

To address these limitations, extensive research has focused on two aspects, corresponding to the two stages in the mmWave radar signal processing pipeline: First, improving

pre-processing methods to enhance the angular resolution of the point cloud, reduce false detections, and improve data quality [5]–[7]. Second, post-processing enhances the geometric and detailed information of the point cloud while reducing the workload on the detector. Such methods still perform worse than LiDAR point clouds in terms of accuracy and density, limiting their suitability for backend tasks in various robotic systems. Therefore, the enhancement of mmWave radar remains an open problem.

Since the requirement of generating high-quality mmWave radar point clouds from raw information is reducing noise and filling sparse areas, the mmWave radar enhancement task can be regarded as a super-resolution task. Thus, the application of diffusion models to mmWave radar is quite natural. For example, Zhang et al. [7] apply RAH as the 2D representation of mmWave radar and successfully generate BEV maps of LiDAR-like quality. Luan et al. [8] then explore the BEV in mmWave radar super-resolution. Frustratingly, both RAH and BEV are not intuitive for humans due to the focus on velocity information and top view, respectively. Hence, the diffusion models pre-trained on massive natural image datasets cannot fully perform super-resolution generation on these 2D proxy representations.

To overcome this problem, we propose a novel method that pioneers the application of fusing range images with image diffusion models. Unlike other representations, range images preserve more geometric and semantic information while aligning better with human perceptual patterns and natural images, which can be intuitively observed in Fig. 1. This enables the efficient transfer of knowledge from pre-trained image diffusion models to address the super-resolution task, thereby significantly enhancing the performance and efficiency of the mmWave radar enhancement.

To validate the effectiveness of our approach, we conducted extensive benchmark comparisons against existing methods on both public datasets and our self-constructed datasets. The results show that our approach significantly outperforms existing methods in terms of mmWave radar point cloud quality, confirming the superior performance of our approach.

In summary, the main contributions of this paper are as follows:

- 1) We propose a novel high-quality mmWave radar point cloud generation method based on a pre-trained diffusion model that can generate truly three-dimensional dense and accurate LiDAR-like point clouds.
- 2) Our work pioneers the integration of range image representations with diffusion models for mmWave radar super-resolution. By introducing human perception-aligned range images as a proxy representation of point clouds, we can fully leverage the prior knowledge embedded in pre-trained models.
- 3) We conducted extensive benchmark comparisons with other methods on both public and self-constructed datasets, which validated the superior performance of the proposed approach.

II. RELATED WORK

Traditional detection methods such as constant false alarm rate (CFAR) [9]–[12] and multiple signal classification (MUSIC) [13] generate point clouds that are either excessively sparse or have low signal-to-noise ratios. Existing research on improving the quality of mmWave radar point clouds primarily focuses on improving pre-processing methods and post-processing methods.

A. Pre-processing Methods

Cheng et al. [5] generated ground truth Range-Doppler Maps (RDM) from LiDAR point clouds and used them to train Generative Adversarial Networks (GANs) for building detectors. While this approach improves detection performance over traditional methods, it still relies on traditional DOA estimation, leading to noisy mmWave radar point clouds. Prabhakara et al. [6] supervised a U-Net network using LiDAR point cloud labels, with low-resolution radar 2D heatmaps as input, to directly generate LiDAR-like point clouds. This approach retains real object data in the scene while eliminating part of the noise. Zhang et al. [7] supervised a diffusion model using LiDAR BEV images, which predicts LiDAR-like BEV images from paired radar RAH. This method can denoise and densify mmWave data at the same time. The two methods mentioned above use neural networks’ cross-modal learning to directly generate more accurate and dense point cloud data without DOA estimation. However, neither method can generate true 3D point clouds, which limits their applicability for higher-level tasks such as autonomous navigation in complex environments.

B. Post-processing Methods

Lu et al. [14] proposed MilliMap, which uses a GAN and takes sparse maps obtained from Bayesian grid mapping as input. This method can reconstruct dense grid maps. Geng et al. [15] first applied non-coherent integration and synthetic aperture accumulation methods to improve the density and angular resolution of radar point clouds, and then proposed the RDM network, which further filters out noise under the guidance of LiDAR point clouds. However, both methods rely on accurate ego-motion estimation from other sensors, which is difficult to obtain in extreme environments. Cai et al. [16] combined traditional signal processing with an adaptive neural network to generate high-quality indoor point clouds from mmWave reflection signals. Although this method integrates mmWave data collected from multiple devices, the resulting point clouds still lack sufficient geometric shape and detailed information. Lu et al. [17] proposed an innovative DNN-based odometry method that estimates self-motion through mmWave radar and IMU. This method jointly optimizes the transformation estimation and latent feature relationships between successive sampling intervals, effectively extracting useful motion information from complex sensor data. Zhuang et al. [18] proposed an incremental non-convex method instead of the traditional RANSAC approach for mapping with mmWave radar and inertial odometry, enabling robust and efficient self-velocity

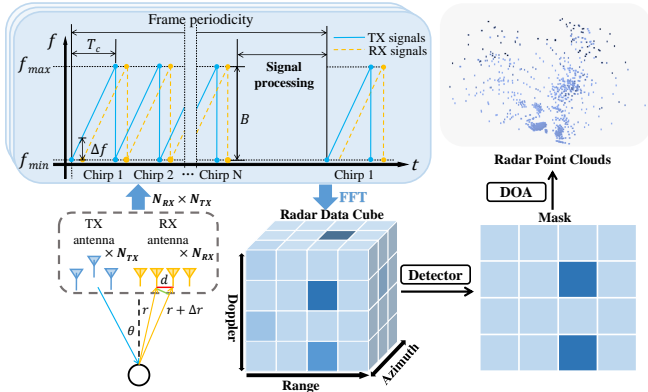


Fig. 2. Illustration of point clouds generated from the raw ADC data of mmWave radar.

estimation from a single scan. However, both methods require the introduction of IMU sensors to achieve self-motion estimation in conjunction with mmWave radar.

In summary, existing methods either require fusion with other sensors to overcome the limitations of mmWave radar, or the generated point clouds are still not dense or accurate enough, making it challenging to support autonomous navigation or other advanced tasks in complex environments.

III. PRELIMINARIES

A. MmWave Radar Signal Processing

With the advancement of mmWave radar technology, it has transitioned from the conventional single-input single-output (SISO) radar to the more sophisticated multi-input multi-output (MIMO) radar. MIMO radar is outfitted with an array of multiple transmit and receive antennas, significantly improving spatial resolution, signal quality, and adaptability.

A frame of transmitted signals in mmWave radars comprises N_{chirp} linear frequency-modulated chirps, with frequencies ranging from f_{min} to f_{max} . Each chirp lasts for a duration of T_c and possesses a bandwidth of $B = f_{max} - f_{min}$. The reflected signal and the transmitted signal are subsequently mixed via a mixer to produce an intermediate frequency (IF) signal, which is then sampled by a sampler to generate a 4D data cube. The four dimensions of this data cube correspond to the sampling of distinct transmitting antennas, receiving antennas, chirps, and time intervals.

The two-dimensional data from a single transmitting antenna and a single receiving antenna within the radar data cube is processed through the Fast Fourier Transform (FFT) to derive the RDM. Distinct range and Doppler bins correspond to targets situated at varying distances and velocities relative to the mmWave radar. The range of objects is determined using the formula $r = \Delta f c / 2S$, where Δf denotes the frequency shift between the received and transmitted signals, representing the frequency of the IF signal, c is the speed of light, and S is the slope of the FMCW signal. The maximum measurable distance is given by $r_{max} = cB / 2S$, and the range resolution can be calculated as $r_{res} = c / 2B$.

The velocity of the target is derived from the phase shift of the IF signal and can be expressed as $v = (\Delta\phi_v)\lambda / (4\pi T_c)$,

where $\Delta\phi_v$ represents the phase shift obtained from a second FFT, commonly referred to as the Doppler FFT, and λ is the wavelength.

The RDM obtained through the aforementioned method contains considerable noise, necessitating the use of detectors such as CFAR to identify targets. The azimuth and elevation angles of each target are determined by the data corresponding to the same position in the RDM, which is derived from different transmitting and receiving antennas. Due to the minimal difference in distance between the target and the various antennas, the frequency shift of the IF signal is small, but the phase shift remains substantial. Consequently, the azimuth and elevation angles of the target can be calculated using the formula $\theta = \arcsin(\lambda(\Delta\phi_a) / 2\pi d)$, where d represents the distance between the RX antennas, typically half the wavelength λ , and $\Delta\phi_a$ denotes the phase shift obtained from a third FFT, commonly referred to as the Angle FFT. Importantly, from this angle calculation formula, the angular resolution can be expressed as $\theta_{res} = \lambda / (N_T N_R d \cos(\theta))$, where N_T and N_R are the numbers of TX and RX antennas, respectively. This illustrates that the primary method for enhancing the angular resolution of an FMCW radar is by increasing the number of antennas.

The mmWave radar coordinates (x, y, z, v) are derived from the range, velocity, azimuth angle, and elevation angle corresponding to the detected unit, as outlined above. The entire signal processing flow of the mmWave radar is depicted in Fig. 2.

B. Diffusion Models

Diffusion models can be encapsulated within a unified generative modeling framework proposed by Karras et al. [19]. They conceptualize the diffusion process, which is represented as a stochastic differential equation (SDE):

$$dx = f(t)x dt + g(t) d\omega_t, \quad (1)$$

where ω_t denotes the standard Wiener process, $f(\cdot) : \mathbb{R} \rightarrow \mathbb{R}$ and $g(\cdot) : \mathbb{R} \rightarrow \mathbb{R}$ represent the drift and diffusion coefficients, respectively, with d indicating the dimensionality of the dataset.

The diffusion model learns to reverse a forward diffusion process, which corresponds to the forward SDE in Eq. 1 and is defined as follows:

$$q(x_t | x_0) := \mathcal{N}(x_t; s(t)x_0, s^2(t)\sigma^2(t)\mathcal{I}), \quad (2)$$

where $q(\cdot | \cdot)$ represents the conditional probability, $\mathcal{N}(x; \mu, \Sigma)$ denotes the probability density function of $\mathcal{N}(\mu, \Sigma)$ evaluated at x , $t \in \{1, \dots, T\}$, where T is the total number of steps in the diffusion chain, $s(t) = \exp\left(\int_0^t f(\xi) d\xi\right)$, and $\sigma(t) = \sqrt{\int_0^t \frac{g(\xi)^2}{s(\xi)^2} d\xi}$. Gaussian noise can be added to x_0 to yield any x_t in a single step. The forward process models a fixed Markov chain, and the noise depends on a variance schedule $s^2(t)\sigma^2(t)$.

The reverse process is defined by the following formula, with parameters θ :

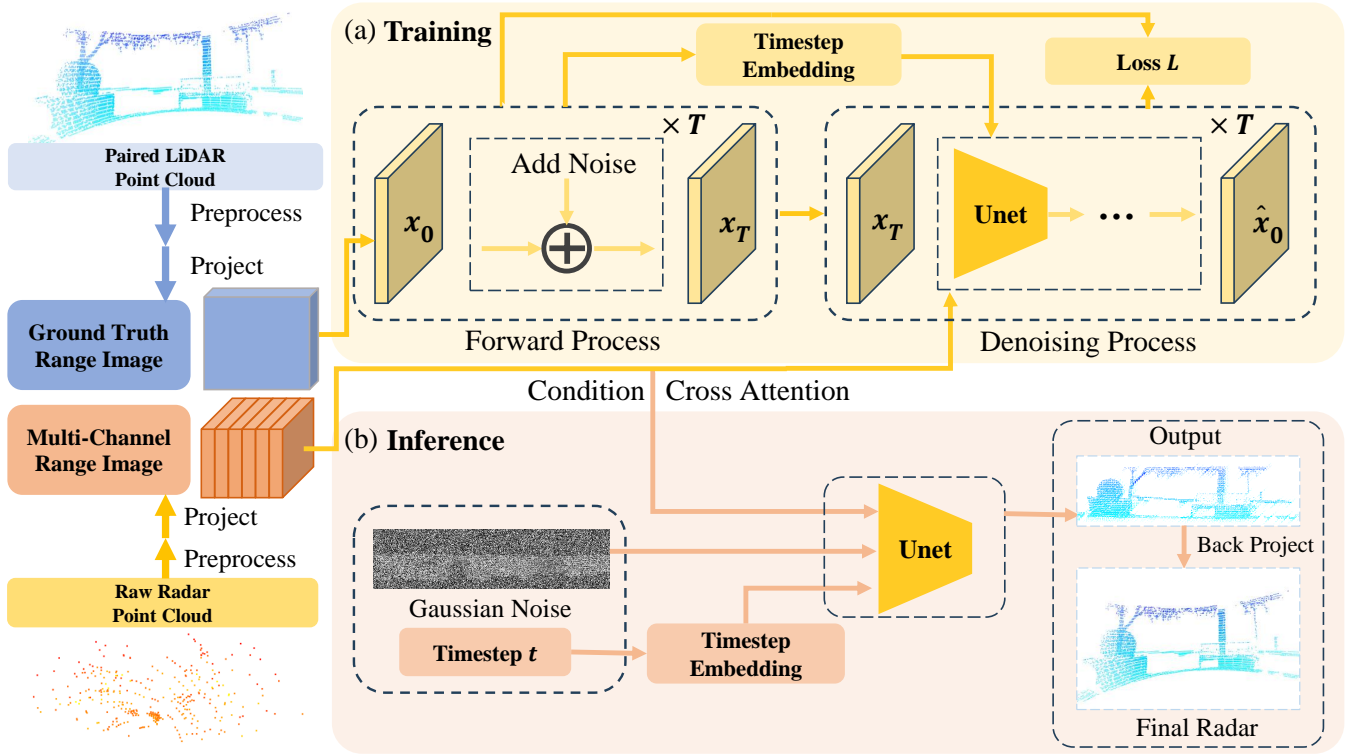


Fig. 3. Diagram of the architecture of our proposed approach. (a) In training, the ground truth LiDAR point cloud and the raw mmWave radar point cloud are respectively projected into the range image x_0 and the multi-channel range image c . Then x_0 are corrupted to x_T through the forward process. Finally, the neural network is trained to estimate the ground truth range image, conditioned on the paired radar multi-channel range images. (b) In inference, the neural network directly predicts \hat{x}_0 from pure Gaussian noise conditioned on the paired radar multi-channel range images. Subsequently, the predicted range image \hat{x}_0 is back-projected to obtain the final high-quality mmWave radar point cloud.

$$p_{\theta}(x_0) := \int p_{\theta}(x_{0:T}) dx_{1:T}, \quad (3)$$

$$p_{\theta}(x_{0:T}) = p(x_T) \prod_{t=1}^T p_{\theta}(x_{t-1}|x_t), \quad (4)$$

$$p_{\theta}(x_{t-1}|x_t) := \mathcal{N}(x_{t-1}; \mu_{\theta}(x_t, t), \Sigma_{\theta}(x_t, t)). \quad (5)$$

By employing a fixed variance $\Sigma_{\theta}(x_t, t)$, our task reduces to learning the means of the reverse process, $\mu_{\theta}(x_t, t)$. Training is conventionally carried out through a reweighted variational bound on the maximum likelihood objective, with the loss defined as follows:

$$L := \mathbb{E}_{t,q} \left[\lambda_t \|\mu_t(x_t, x_0) - \mu_{\theta}(x_t, t)\|^2 \right], \quad (6)$$

where $\mu_t(x_t, x_0)$ is the mean of the forward process posterior $q(x_{t-1}|x_t, x_0)$.

IV. METHODS

This section specifically details the proposed method. In recent years, image diffusion models, trained on massive image pairs, have significantly advanced the field of image super-resolution, inspiring us to leverage research from this domain to tackle point cloud super-resolution tasks. Consequently, we integrate range images with diffusion models. Specifically, the range image projected from the LiDAR point cloud is used to supervise the training of the diffusion model, after which high-quality range images

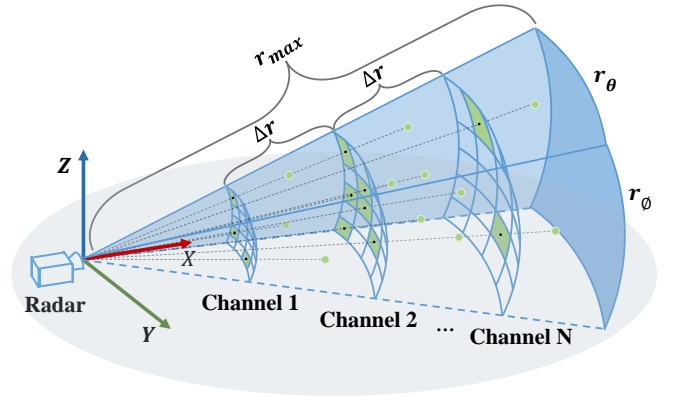


Fig. 4. Illustration of multi-channel range image point cloud proxy representation for mmWave Radar.

are restored from noise, conditioned by multi-channel range data from mmWave radar. Ultimately, the range image is back-projected to generate high-quality mmWave radar point clouds. The system architecture is illustrated in Fig. 3.

A. Range Image Construction

Certain LiDAR systems, such as Velodyne, generate raw data in a format that resembles range images. Each column represents the distances measured by laser range-finders at a specific moment, while each row corresponds to varying rotational angles of the sensors. This implies that range images can serve as a proxy for point clouds. A range image, in essence, is a 2D array where each pixel contains the

spherical coordinates and range of a point mapped onto its field of view. We transform each point $\Pi : \mathbb{R}^3 \rightarrow \mathbb{R}^2$ through the mapping $\mathbf{p}_i = (p_x, p_y, p_z)$ into spherical coordinates, and then into image coordinates, as follows:

$$\begin{pmatrix} i_\theta \\ i_\phi \end{pmatrix} = \begin{pmatrix} \lfloor (\arctan 2(p_y, p_x) - \theta_{\min}) l_w r_\theta^{-1} \rfloor \\ \lfloor (\arccos(p_z, r) - \phi_{\min}) l_h r_\phi^{-1} \rfloor \end{pmatrix}, \quad (7)$$

where $r = \|\mathbf{p}_i\|_2$ denotes the range of each point, θ_{\min} and ϕ_{\min} represent the minimum values of the azimuth and elevation angles, r_θ and r_ϕ are the ranges of the azimuth and elevation angles, l_w and l_h are the width and height of the range image, and $\lfloor \cdot \rfloor$ denotes the floor function.

B. Data Representation

Furthermore, given the inherent penetration ability of mmWave radar, directly converting the raw mmWave radar point cloud data into range images results in multiple points being projected into the conical region corresponding to each pixel. This phenomenon causes point cloud data at greater radial distances to become occluded, leading to data loss and increased sparsity of the mmWave radar data. To mitigate this, we perform slicing operations along the range dimension of the mmWave radar point cloud and individually map the radar data from each slice, thus generating multi-channel range images. The process of constructing multi-channel range images is illustrated in Fig. 4.

Notably, the resolution of the range image is critically important. If the resolution is too low, significant amounts of critical information are lost during the point cloud mapping process. Conversely, excessively high resolution can result in an overly complex model architecture, placing undue computational strain and complicating subsequent training. For mmWave radar, which produces relatively unordered point cloud data, some information loss is inevitable during the mapping to range images. To strike a balance between model capacity and information retention, we carefully assess the amount of preserved information at various range image resolutions, ultimately selecting an optimal resolution. In contrast, the raw LiDAR point cloud, with its angular resolution and relatively organized spatial distribution, allows for the conversion to range images with minimal loss when a resolution approximating the LiDARs angular resolution is chosen.

C. Diffusion-Based Range Image Prediction

As elaborated in Section III-B, the principal objective of the diffusion model is to learn the reverse process of the forward diffusion mechanism, which incrementally introduces noise to data samples according to the predefined noise schedule described in Eq. 2, where $s(t) = 1$ and $\sigma(t) = t$. Given a set of LiDAR range images x_0 and multi-channel radar range images c that are aligned both spatially and temporally, Gaussian noise is introduced and propagated to x_t . We follow the parameterization approach for the reverse process proposed by Karras et al. [19] to model the original data sample $D_\theta(x_t, t, c)$ conditioned on c . During the inference stage, we perform deterministic

sampling using the probabilistic flow (PF) ODE defined by Eq. 1 to accelerate the inference process. The Heun method is employed for iterative solving. The PF ODE is defined as follows:

$$dx = -\dot{\sigma}(t)\sigma(t)\nabla_x \log p(x; \sigma(t))dt, \quad (8)$$

where the dot denotes a time derivative, $\nabla_x \log p(x; \sigma(t))$ represents the score function.

1) *Design of the Network Architecture:* The resolutions of range images from LiDAR and mmWave radar differ due to distinct point cloud densities. If the range images of the mmWave radar are directly concatenated with the noise at the input layer, size alignment through methods such as interpolation becomes necessary, leading to the inevitable loss of information. Consequently, we opt to embed conditions during the downsampling stage, thereby ensuring the maximum retention of the original data. Furthermore, as the pitch range of LiDAR is narrower than its horizontal range, the height and width of its range images are unequal. Thus, we introduce a horizontal sampling module, which effectively extracts the lateral features of the target, adjusts the feature dimensions, and accelerates the feature extraction process simultaneously.

2) *Training Objective:* We first optimize the following Mean Squared Error (MSE) loss to make $D_\theta(x_t, t, c)$ similar to x_0 . The MSE loss is expressed as follows:

$$L_m = \|x_0 - D_\theta(x_t, t, c)\|_2^2. \quad (9)$$

However, since MSE loss is particularly sensitive to outliers, it may lead the model to overly focus on the few anomalous pixels within the image, thereby ignoring the broader enhancement in image quality. To mitigate this issue, we introduce the Learned Perceptual Image Patch Similarity (LPIPS) [20], which leverages a pre-trained deep network to extract features from both x_0 and $D_\theta(x_t, t, c)$. and then calculates the distance between these features to evaluate the perceptual similarity between the images. The LPIPS loss is articulated as follows:

$$L_p = \|g_p(x_0) - g_p(D_\theta(x_t, t, c))\|_2^2. \quad (10)$$

Furthermore, when transforming point clouds into range images, while the loss of geometric information remains negligible, it cannot be eliminated. To mitigate this geometric loss, drawing inspiration from the per-point coordinate supervision method in [7], we introduce per-pixel distance supervision. This involves calculating the distance loss for each pixel based on the predicted distance at each pixel location.

$$L_c = |x_0 - D_\theta(x_t, t, c)|. \quad (11)$$

Finally, our loss function consists of three components.

$$L = \lambda_m L_m + \lambda_p L_p + \lambda_c L_c. \quad (12)$$

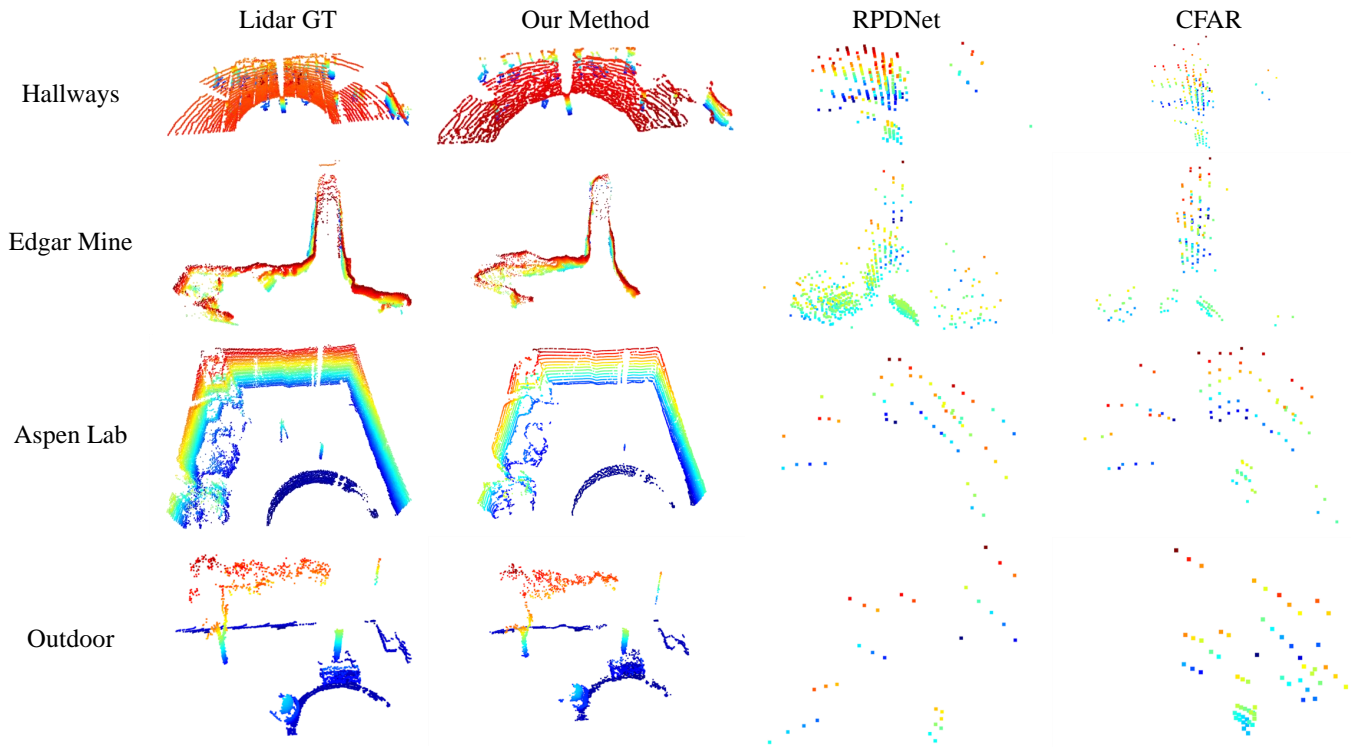


Fig. 5. Qualitative comparisons of single-frame 3D point clouds conducted on the ColoRadar dataset. The LiDAR ground truth and the 3D mmWave radar point clouds generated by each method in the Hallway, Edgar Mine, Aspen Lab, and Outdoor scenes are shown above. A multi-color rendering scheme is employed for visualizing the point clouds, with red hues representing higher elevations. To enhance clarity, the visualization size of the point clouds from the RPDNet [5] and OS-CFAR [12] methods is scaled by a factor of two. Among the various CFAR methods [9]–[12], only the OS-CFAR [12], exhibiting superior performance, is visualized.

TABLE I
QUANTITATIVE RESULTS ON THE COLORADAR DATASET. THE **BOLD** DENOTES THE BEST PERFORMANCE.

Method	Hallways			Edgar Mine			Aspen Lab			Outdoor		
	CD(m) ↓	MHD(m) ↓	F-Score(%) ↑	CD(m) ↓	MHD(m) ↓	F-Score(%) ↑	CD(m) ↓	MHD(m) ↓	F-Score(%) ↑	CD(m) ↓	MHD(m) ↓	F-Score(%) ↑
SO-CFAR [9]	12.841	2.671	15.5	11.070	2.705	14.9	17.160	6.154	13.3	21.547	10.80	11.5
CA-CFAR [10]	9.417	1.137	18.8	12.715	4.502	11.4	8.725	1.827	14.3	10.044	1.580	16.0
GO-CFAR [11]	8.356	1.115	19.5	11.507	4.194	11.6	8.097	2.271	14.2	9.946	1.295	15.6
OS-CFAR [12]	8.326	0.976	20.7	8.209	3.844	12.2	5.652	0.887	20.8	8.987	2.421	19.0
RPDNet [5]	2.754	0.339	34.4	2.434	0.760	29.4	2.833	0.717	31.5	8.183	2.203	24.3
Ours	2.247	0.275	44.0	0.413	0.041	78.7	1.024	0.113	62.5	8.196	2.004	25.2

TABLE II
QUANTITATIVE RESULTS ON THE SELF-CONSTRUCTED DATASET.
THE **BOLD** DENOTES THE BEST PERFORMANCE.

Method	Corridor			Hall		
	CD(m) ↓	MHD(m) ↓	F-Score(%) ↑	CD(m) ↓	MHD(m) ↓	F-Score(%) ↑
SO-CFAR [9]	15.606	2.267	5.7	18.368	2.733	4.7
CA-CFAR [10]	11.900	4.144	3.2	11.738	4.459	4.1
GO-CFAR [11]	6.027	2.923	0.6	13.976	10.356	0.9
OS-CFAR [12]	15.928	1.736	6.4	12.562	1.361	8.6
RPDNet [5]	10.278	1.392	6.6	6.844	1.705	14.5
Ours	4.743	1.411	29.4	2.682	0.196	32.7

where $\lambda_m, \lambda_p, \lambda_c$ denotes the weight coefficients of each loss function, used to balance multi-objective optimization during model training

V. EXPERIMENTS AND RESULTS

In this section, we compare the proposed method against baseline methods on both the public dataset (Coloradar) and the self-constructed dataset to validate the superior performance of our approach.

A. Benchmark Comparisons

We performed benchmark comparisons with five baseline methods, including RPDNet [5], SO-CFAR [9], CA-CFAR

[10], GO-CFAR [11], and OS-CFAR [12]. All of these methods, like the one we propose, are capable of generating authentic 3D point clouds. We excluded comparisons with the diffusion model-based methods proposed by Zhang et al. [7] and Luan et al. [8], as these methods are solely designed to generate high-quality BEV maps.

1) *Dataset*: The ColoRadar dataset provides LiDAR point cloud data and raw mmWave ADC data for seven different environments, including indoor scenes (Arpg Lab, Ec Hallways, and Aspen Corporation), outdoor scenes (Longboard and Outdoor), and mining environments (Edgar Army and Edgar Classroom). Each environment contains multiple trajectories. We use the first three trajectories of each scene as the training set, while the remaining trajectories are used as the test set. In addition, using the handheld data collection platform shown in Fig. 7, we respectively collected four trajectories in the hall and corridor of the Robotics Institute of Zhejiang University, totaling 6,636 frames. Similarly, we set the first three trajectories of each scene as the training set, and the others as the testing set.

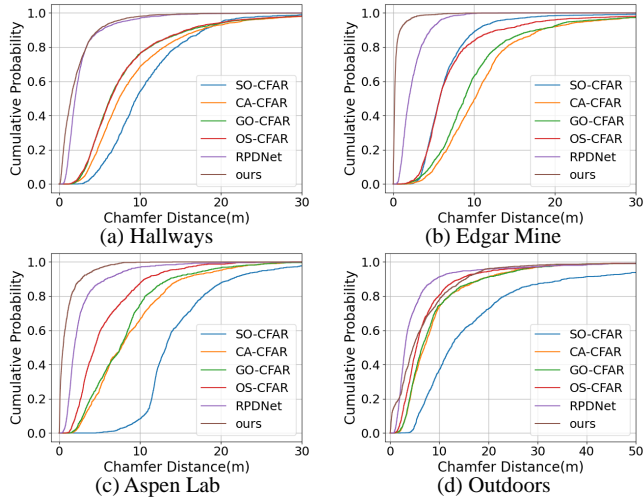


Fig. 6. The CDF curves of our method and the baseline methods on the ColoRadar dataset.

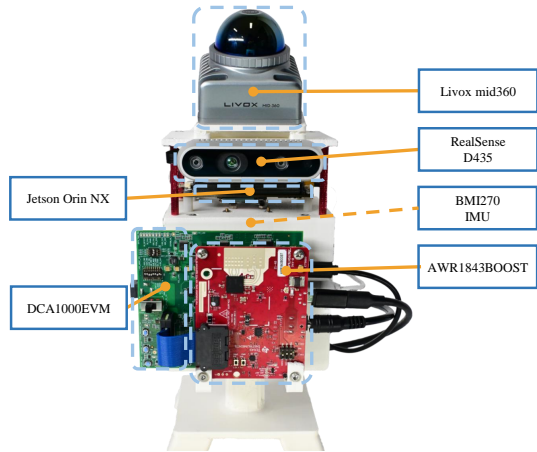


Fig. 7. Our customized handheld data collection platform. The LiDAR is mounted at an inclined angle to align with the field of view of the mmWave radar.

2) *Data Collection Platform*: We customized a handheld data collection platform, as shown in Fig. 7. It consists of an NVIDIA Jetson Orin NX for recording sensor data, a forward-tilted Livox Mid-360 LiDAR, and a BMI270 IMU to estimate real-time platform poses with the assistance of Fast-LIO [21] for visualization. Additionally, it is equipped with a TI-AWR1843BOOST and TI-DCA1000EVM for collecting mmWave radar raw data, and an Intel RealSense Depth Camera D435 to capture image data for visualization.

3) *Preprocessing*: Due to the different operational ranges of mmWave radar and LiDAR, we preprocessed the raw sensor data. First, we used the extrinsic calibration matrix of the two sensor coordinate systems to achieve spatial alignment of the data. Subsequently, we obtained the shared field of view of the two sensors and removed data outside the range. In addition, due to the low reflectivity of surfaces such as floors and indoor ceilings, these objects are usually not perceived by millimeter wave radar. Therefore, we applied Patchwork++ [22] to remove these point clouds from the LiDAR data, where the ceiling is removed by flipping the

Z-axis and applying Patchwork++ again.

Additionally, considering that mmWave radar is not sensitive to low-reflectivity objects, we first employed DBSCAN to cluster the combined point cloud of mmWave radar and LiDAR. Then, We applied additional filtering to the LiDAR point cloud using labels from mmWave radar to eliminate objects that are difficult for the mmWave radar to detect. This step ensures that the neural network does not learn features undetectable by mmWave radar, thereby preventing the neural network from being misled during training.

4) *Implementation*: In the process of mmWave point cloud processing, we employed the mmWave radar signal processing techniques described in Section III, alongside the CFAR detector, to acquire the raw mmWave radar point cloud data. The performance of the CFAR detector is notably influenced by the threshold setting. A higher threshold enables superior denoising performance; however, it also leads to a loss of information. Under such conditions, it becomes nearly impossible to match the density of the mmWave radar point cloud to that of LiDAR point clouds. Therefore, to preserve as much raw mmWave radar information as possible, we configured the CFAR detectors threshold to approach zero.

To balance model capacity and information, we set the range image resolution of LiDAR and radar to 128×512 and 64×64 , respectively. We adopted the same diffusion noise and timestamp settings as the EDM proposed by Karras et al. [19], and used the Heun deterministic sampler for sampling.

B. Qualitative Comparison

The mmWave radar point clouds generated by both the proposed and baseline methods, alongside the ground truth LiDAR point clouds, are presented in Fig. 1 and Fig. 5. The results demonstrate that our method outperforms all baseline methods in terms of both denoising capability and densification across all scenes. Our method achieves remarkable reconstruction of the curved features of rock walls in mining environments, as well as the sharp corner features in intricate environments. Among the baseline methods, OS-CFAR [12], a traditional technique for processing mmWave data, estimates noise levels by sorting the signal intensity within the observation window to adjust the detection threshold. However, it is highly susceptible to outliers, leading to poor detection performance. In contrast, RPDNet [5] utilizes LiDAR point clouds to assist in training a GAN, thereby enabling it to eliminate more clutter and detect more targets. Nevertheless, RPDNet [5] still relies on traditional DOA estimation methods, resulting in outputs that contain considerable noise.

C. Quantitative Comparison

We begin by presenting the evaluation metrics employed in our quantitative comparison: Chamfer Distance (CD), Modified Hausdorff Distance (MHD), and F-Score. CD quantifies the global similarity between two point clouds by summing the distances from each point to the nearest point in the other point cloud. MHD evaluates the maximum disparity between two point clouds by calculating their forward and backward

Hausdorff distances. F-Score, defined as the harmonic mean of precision P and recall R , is utilized to assess the quality of point cloud reconstruction. The results of the quantitative analysis are provided in Tab.I and Tab.II, while Fig. 6 illustrates the cumulative distribution function (CDF) curves of the Chamfer Distance.

The results demonstrate that the proposed method significantly outperforms the baseline approaches across all scenes in both datasets. The RPDNet [5] method is only marginally comparable to the proposed approach concerning the CD metric in the Outdoor scenes of the ColoRadar dataset and the MHD metric in the Corridor scenes of the self-constructed dataset. This arises from the inherent complexity of the Outdoor scene, which is populated by numerous targets exhibiting low reflectivity and small sizes, thus hindering the ability of mmWave radar to effectively observe these objects, thereby affecting the model's performance. Furthermore, The Corridor scene in the self-constructed dataset contains a significant amount of glass. The smooth texture of glass has the potential to deflect millimeter waves in various directions, generating virtual images, while the multi-layered glass structures may cause multiple reflections of the radar signals, resulting in interference that detracts from the efficacy of the proposed method.

VI. CONCLUSION

This paper proposes a novel approach for generating high-quality mmWave radar point clouds. By fully leveraging the powerful generation capability of the diffusion model, the proposed method can effectively process the sparse and noisy original mmWave radar point cloud of a single frame and obtain an accurate and dense point cloud similar to LiDAR. Our approach employs range images aligned with human perception as proxy representations for point clouds and combines them with image diffusion models for the first time to solve this task. Owing to the projection that aligns with human perception, the range image representation closely resembles natural images, thereby facilitating the transfer of knowledge from the pre-trained image diffusion model and substantially enhancing overall performance. The proposed method is validated on public and self-constructed datasets, significantly outperforming baseline methods in terms of both point cloud quality and density.

In the future, we intend to explore the interdependencies between adjacent frames of mmWave radar data to further enhance the interframe continuity of mmWave radar point clouds. This is of great significance for applying mmWave radar to advanced tasks such as autonomous robot navigation.

REFERENCES

- [1] Y. Lyu, L. Hua, J. Wu, X. Liang, and C. Zhao, "Robust radar inertial odometry in dynamic 3d environments," *Drones*, vol. 8, no. 5, p. 197, 2024.
- [2] J. Zhang, H. Zhuge, Z. Wu, G. Peng, M. Wen, Y. Liu, and D. Wang, "4dradarslam: A 4d imaging radar slam system for large-scale environments based on pose graph optimization," in *2023 IEEE International Conference on Robotics and Automation (ICRA)*, pp. 8333–8344, IEEE, 2023.
- [3] R. Guan, S. Yao, X. Zhu, K. L. Man, E. G. Lim, J. Smith, Y. Yue, and Y. Yue, "Achelous: A fast unified water-surface panoptic perception framework based on fusion of monocular camera and 4d mmwave radar," in *2023 IEEE 26th International Conference on Intelligent Transportation Systems (ITSC)*, pp. 182–188, IEEE, 2023.
- [4] Y. Cheng, H. Xu, and Y. Liu, "Robust small object detection on the water surface through fusion of camera and millimeter wave radar," in *Proceedings of the IEEE/CVF international conference on computer vision*, pp. 15263–15272, 2021.
- [5] Y. Cheng, J. Su, M. Jiang, and Y. Liu, "A novel radar point cloud generation method for robot environment perception," *IEEE Transactions on Robotics*, vol. 38, no. 6, pp. 3754–3773, 2022.
- [6] A. Prabhakara, T. Jin, A. Das, G. Bhatt, L. Kumari, E. Soltanaghai, J. Bilmes, S. Kumar, and A. Rowe, "High resolution point clouds from mmwave radar," in *2023 IEEE International Conference on Robotics and Automation (ICRA)*, pp. 4135–4142, IEEE, 2023.
- [7] R. Zhang, D. Xue, Y. Wang, R. Geng, and F. Gao, "Towards dense and accurate radar perception via efficient cross-modal diffusion model," *arXiv preprint arXiv:2403.08460*, 2024.
- [8] K. Luan, C. Shi, N. Wang, Y. Cheng, H. Lu, and X. Chen, "Diffusion-based point cloud super-resolution for mmwave radar data," in *2024 IEEE International Conference on Robotics and Automation (ICRA)*, pp. 11171–11177, 2024.
- [9] M. Barkat, S. Himonas, and P. Varshney, "Cfar detection for multiple target situations," in *IEE Proceedings F (Radar and Signal Processing)*, vol. 136, pp. 193–209, IET, 1989.
- [10] G. Minkler and J. Minkler, "Cfar: the principles of automatic radar detection in clutter," *Nasa sti/recon technical report a*, vol. 90, p. 23371, 1990.
- [11] P. P. Gandhi and S. A. Kassam, "Analysis of cfar processors in nonhomogeneous background," *IEEE Transactions on Aerospace and Electronic systems*, vol. 24, no. 4, pp. 427–445, 1988.
- [12] H. Rohling, "Radar cfar thresholding in clutter and multiple target situations," *IEEE transactions on aerospace and electronic systems*, no. 4, pp. 608–621, 1983.
- [13] R. Schmidt, "Multiple emitter location and signal parameter estimation," *IEEE Transactions on Antennas and Propagation*, vol. 34, no. 3, pp. 276–280, 1986.
- [14] C. X. Lu, S. Rosa, P. Zhao, B. Wang, C. Chen, J. A. Stankovic, N. Trigoni, and A. Markham, "See through smoke: robust indoor mapping with low-cost mmwave radar," in *Proceedings of the 18th International Conference on Mobile Systems, Applications, and Services*, pp. 14–27, 2020.
- [15] R. Geng, Y. Li, D. Zhang, J. Wu, Y. Gao, Y. Hu, and Y. Chen, "Dream-pcd: Deep reconstruction and enhancement of mmwave radar pointcloud," *arXiv preprint arXiv:2309.15374*, 2023.
- [16] P. Cai and S. Sur, "Millipcd: Beyond traditional vision indoor point cloud generation via handheld millimeter-wave devices," *Proceedings of the ACM on Interactive, Mobile, Wearable and Ubiquitous Technologies*, vol. 6, no. 4, pp. 1–24, 2023.
- [17] C. X. Lu, M. R. U. Saputra, P. Zhao, Y. Almalioğlu, P. P. De Gusmao, C. Chen, K. Sun, N. Trigoni, and A. Markham, "milliego: single-chip mmwave radar aided egomotion estimation via deep sensor fusion," in *Proceedings of the 18th Conference on Embedded Networked Sensor Systems*, pp. 109–122, 2020.
- [18] Y. Zhuang, B. Wang, J. Huai, and M. Li, "4d iriom: 4d imaging radar inertial odometry and mapping," *IEEE Robotics and Automation Letters*, vol. 8, no. 6, pp. 3246–3253, 2023.
- [19] T. Karras, M. Aittala, T. Aila, and S. Laine, "Elucidating the design space of diffusion-based generative models," *Advances in neural information processing systems*, vol. 35, pp. 26565–26577, 2022.
- [20] R. Zhang, P. Isola, A. A. Efros, E. Shechtman, and O. Wang, "The unreasonable effectiveness of deep features as a perceptual metric," in *Proceedings of the IEEE conference on computer vision and pattern recognition*, pp. 586–595, 2018.
- [21] W. Xu and F. Zhang, "Fast-lio: A fast, robust lidar-inertial odometry package by tightly-coupled iterated kalman filter," *IEEE Robotics and Automation Letters*, vol. 6, no. 2, pp. 3317–3324, 2021.
- [22] S. Lee, H. Lim, and H. Myung, "Patchwork++: Fast and robust ground segmentation solving partial under-segmentation using 3d point cloud," in *2022 IEEE/RSJ International Conference on Intelligent Robots and Systems (IROS)*, pp. 13276–13283, IEEE, 2022.